Electronic Supplementary Information (ESI)

Achievement of High Efficiency with Extremely Low Efficiency Roll-off in Solution-Processed Thermally Activated Delayed Fluorescence OLEDs manufactured using Xanthone-based Bipolar Host Materials

Chae Yeong Kim‡, Chiho Lee‡, Hyung Jong Kim, Jinhyo Hwang, Mallesham Godumala, Ji-Eun Jeong, Han Young Woo, Min Ju Cho*, Sungnam Park* and Dong Hoon Choi*

Department of Chemistry, Research Institute for Natural Sciences, Korea University, 145 Anam-ro, Sungbuk-gu, Seoul 136-701, Korea

E-mail: chominju@korea.ac.kr, spark8@korea.ac.kr, dhchoi8803@korea.ac.kr

‡ These authors contributed equally to this work.

Table of Contents

Experimental Section

Characterization

The ^{1}H and ^{13}C NMR measurements of compounds were performed on Bruker 500 and 125 MHz spectrometers, respectively. The mass spectra of each compound were measured using a MALDI-TOF/TOF™ 5800 system (AB SCIEX) at the Korea Basic Science Institute (Seoul).

Thermal properties, including glass-transition temperature (T_g) and decomposition temperature (T_d), were measured by SCINCO TGA-N 1000 and Mettler DSC 821e instruments under N_2 conditions at a heating rate of 10°C min^{-1}. The cyclic voltammograms of **Xp-mCP** and **Xm-mCP** in were obtained by cyclic voltammetry (CV; EA161, eDAQ) experiments with a 0.10 M electrolyte solution of tetrabutylammonium hexafluorophosphate (Bu_4NPF_6) in acetonitrile. The reference compound was Ag/AgCl; counter electrodes were made of platinum wire electrodes. UV-vis absorption spectra in toluene solutions and film-states were measured using Agilent 8453 spectrophotometer (photodiode array = 190-1100 nm). The photoluminescence (PL) spectra were obtained by Hitachi F-7000 FL spectrophotometer at room temperature (298 K). Low-temperature photoluminescence (LTPL) spectra at 77 K in 2-methyltetrahydrofuran were measured by HITACHI F-7000 fluorescence spectrometer.

The surface morphology of host and dopant blend film was investigated by an atomic force microscope (AFM, XE-100 advanced scanning probe microscope, PSIA). The absolute PL quantum yield (PLQY) was obtained by fluorescence spectrophotometer (JASCO FP-8500) equipment with a Xenon lamp excitation source through the use of an integrating sphere (ILF-835, JASCO) at room temperature under N_2 conditions. The transient PL intensities and exciton lifetimes were measured for doped films of **Xp-mCP** : 20 wt% t4CzIPN and **Xm-mCP** : 20 wt% t4CzIPN. The exciton lifetimes and transient PL were measured by using a train of 1064-nm pulses

of 5-ns duration, produced at 10 Hz from a Nd:YAG laser (Powerlite Precision II 8000, Continuum). A 355-nm pulse was obtained by the generation of the third harmonic and used to directly excite the film sample cast on quartz. The emission from the film sample was collected using a lens (focal length: 10 cm), passed through a monochromator, and detected using a photomultiplier tube (PMT) connected to a 100 MHz digital oscilloscope (DSO-X 3014A, Keysight). The prompt and delayed emissive components were identified using single- and triple-exponential decaying functions.

Determination of all rate constants associated with thermally activated delayed fluorescence kinetics of a dopant with a relatively small PL quantum yield

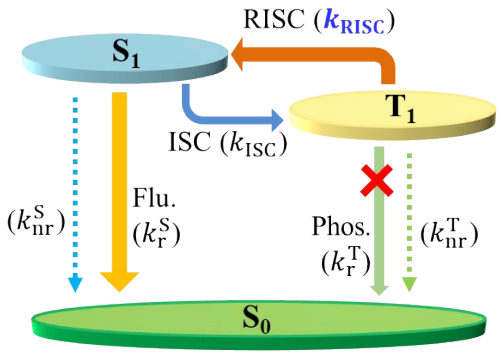

The TADF kinetics associated with the lowest singlet excited state (S_1), triplet excited state (T_1), and singlet ground state (S_0) can be described as shown in above figure. The coupled differential equations for the populations of S_1 and T_1 states are written as

$$\frac{d[S_1]}{dt} = -(k_r^S + k_{nr}^S + k_{ISC})[S_1] + k_{RISC}[S_1]$$

$$\frac{d[T_1]}{dt} = k_{ISC}[S_1] - (k_{nr}^T + k_{RISC})[T_1]$$

where k_r^S is the rate constant for the radiative decay from the first singlet excited state (S_1). k_{ISC} and k_{RISC} are the rate constants for the intersystem crossing (ISC) and reverse intersystem crossing

(RISC) between S_1 and T_1 states, respectively. k_{nr}^{T} and k_{nr}^{S} are the rate constants for the non-radiative decay from the T_1 and S_1 state, respectively. On solving the above coupled differential equations for $[S_1]$, the following equation should be reached.

$$[S_1] = A_{PF}\exp(-k_{PF}t) + A_{DF}\exp(-k_{DF}t),\ A_{PF} + A_{DF} = 1$$

$$k_{PF}, k_{DF} = \frac{k_r^S + k_{nr}^S + k_{ISC} + k_{nr}^T + k_{RISC}}{2} \times \left(1 \pm \sqrt{1 - \frac{4(k_r^S + k_{nr}^S + k_{ISC})(k_{nr}^T + k_{RISC}) - 4k_{ISC}k_{RISC}}{(k_r^S + k_{nr}^S + k_{ISC} + k_{nr}^T + k_{RISC})^2}} \right)$$

Because the rate constants associated with the singlet excited state are significantly larger than those with the triplet excited state (i.e., $k_r^S, k_{nr}^S, k_{ISC} \gg k_{nr}^T, k_{RISC}$), k_{PF} and k_{DF} can be approximately written as:

$$k_{PF} = k_r^S + k_{nr}^S + k_{ISC}$$

$$k_{DF} = k_{nr}^T + \left(1 - \frac{k_{ISC}}{k_r^S + k_{nr}^S + k_{ISC}} \right) k_{RISC} = k_{nr}^T + \left(1 - \frac{k_{ISC}}{k_{PF}} \right) k_{RISC}$$

The quantum efficiencies of prompt fluorescence (PF) and delayed fluorescence (DF) are given by

$$\Phi_{PF} = \frac{k_r^S}{k_r^S + k_{nr}^S + k_{ISC}} = \frac{k_r^S}{k_{PF}}$$

$$\Phi_{DF} = \sum_{k=1}^{\infty} \left(\Phi_{ISC}\Phi_{RISC} \right)^k \Phi_{PF} = \frac{\Phi_{ISC}\Phi_{RISC}}{1 - \Phi_{ISC}\Phi_{RISC}} \Phi_{PF}$$

where Φ_{PF} and Φ_{DF} are the quantum yield for the prompt and delayed fluorescence, respectively. The quantum efficiencies for the nonradiative relaxation, ISC, and RISC, are given by:

$$\Phi_{nr}^S = \frac{k_{nr}^S}{k_r^S + k_{nr}^S + k_{ISC}} = \frac{k_{nr}^S}{k_{PF}}$$

$$\Phi_{\mathrm{ISC}} = \frac{k_{\mathrm{ISC}}}{k_{\mathrm{r}}^{\mathrm{S}} + k_{\mathrm{nr}}^{\mathrm{S}} + k_{\mathrm{ISC}}} = \frac{k_{\mathrm{ISC}}}{k_{\mathrm{PF}}}$$

$$\Phi_{\mathrm{RISC}} = \frac{k_{\mathrm{RISC}}}{k_{\mathrm{nr}}^{\mathrm{T}} + k_{\mathrm{RISC}}}$$

In the case that the non-radiative relaxation of the triplet state ($k_{\mathrm{nr}}^{\mathrm{T}}$) is significantly slower than k_{RISC} (i.e., $k_{\mathrm{RISC}} \gg k_{\mathrm{nr}}^{\mathrm{T}}$), $\Phi_{\mathrm{RISC}} = \frac{k_{\mathrm{RISC}}}{k_{\mathrm{nr}}^{\mathrm{T}} + k_{\mathrm{RISC}}} \simeq 1$ and $\Phi_{\mathrm{DF}} \simeq \frac{\Phi_{\mathrm{ISC}}}{1-\Phi_{\mathrm{ISC}}}\Phi_{\mathrm{PF}}$. The quantum efficiency for the ISC is approximately obtained by $\Phi_{\mathrm{ISC}} \simeq \frac{\Phi_{\mathrm{DF}}}{\Phi_{\mathrm{PF}} + \Phi_{\mathrm{DF}}}$ where Φ_{PF} and Φ_{DF} are the quantum yield for the prompt and delayed fluorescence, respectively. Therefore, when k_{PF}, k_{DF}, $\Phi_{\mathrm{PF}} = A_{\mathrm{PF}}\Phi_{\mathrm{PL}}$, and $\Phi_{\mathrm{DF}} = A_{\mathrm{DF}}\Phi_{\mathrm{PL}}$ (Φ_{PL}, PLQY) are experimentally determined by measuring the time-dependent PL signal, $[\mathrm{S}_1] = A_{\mathrm{PF}}\exp(-k_{\mathrm{PF}}t) + A_{\mathrm{DF}}\exp(-k_{\mathrm{DF}}t)$ and $A_{\mathrm{PF}} + A_{\mathrm{DF}} = 1$, the rate constants associated with the TADF kinetics of a dopant in host films are readily estimated as:

$$k_{\mathrm{r}}^{\mathrm{S}} = k_{\mathrm{PF}}\Phi_{\mathrm{PF}}$$

$$k_{\mathrm{ISC}} \simeq k_{\mathrm{PF}}\frac{\Phi_{\mathrm{DF}}}{\Phi_{\mathrm{PF}} + \Phi_{\mathrm{DF}}}$$

$$k_{\mathrm{nr}}^{\mathrm{S}} \simeq k_{\mathrm{PF}}\left(1 - \Phi_{\mathrm{PF}} - \frac{\Phi_{\mathrm{DF}}}{\Phi_{\mathrm{PF}} + \Phi_{\mathrm{DF}}}\right)$$

$$k_{\mathrm{RISC}} = \frac{k_{\mathrm{PF}} \cdot k_{\mathrm{DF}}}{k_{\mathrm{ISC}}} \cdot \frac{\Phi_{\mathrm{DF}}}{\Phi_{\mathrm{PF}}}$$

The kinetic model here might be useful to describe the photophysical behavior of a dopant in which the nonradiative relaxation occurs mostly from the singlet excited state (S_1), and the PLQY (Φ_{PL}) is dictated mostly by $k_{\mathrm{nr}}^{\mathrm{S}}$. The dopant molecule (t4CzIPN) used in this work exhibited relatively

small PLQY (Φ_{PL} = 63~66 %), which deviated significantly from 100%. It can be readily assumed that the non-radiative relaxation from S_1 state (k_{nr}^{S}) was responsible for such a low PLQY.

Determination of activation energy, E_a for the reverse intersystem crossing process of a dopant in host films

The films of **Xp-mCP** and **Xm-mCP** with 20% t4CzIPN dopant molecules were placed in a cryostat. The TRPL signals of t4CzIPN in the films were measured at different temperatures (from 200 K to 300 K at intervals of 20 K). At each temperature, the rate constants associated with TADF kinetics could be determined from the TRPL signal as explained in the previous section. Especially, the RISC rate constant was obtained by $k_{RISC} = \frac{k_{PF} \cdot k_{DF}}{k_{ISC}} \cdot \frac{\Phi_{DF}}{\Phi_{PF}}$ at a given temperature. The temperature-dependent RISC rate constant, $k_{RISC}(T)$, can be written using the Arrhenius equation, $\ln k_{RISC}(T) = \ln A - \frac{E_a}{R}\frac{1}{T}$. $\ln k_{RISC}(T)$ was plotted against $1/T$, followed by the activation energy, E_a, for the RISC being determined by the slope, $-E_a/R$.

Computational method

The optimized molecular structure, the frontier molecular orbitals (HOMO and LUMO), and the electronic transition energies of **Xp-mCP** and **Xm-mCP** were calculated by the DFT method with the B3LYP functional and 6-31G(d) basis set implemented in the commercial Gaussian 16 software package[1]. The gap-tuned DFT functional has previously been shown to better estimate the excited state properties (S_1 and T_1 energies) of donor-acceptor type molecules; detailed

computational method have been described in literature.[2-4] Briefly, in this work, we used the ωB97XD functional and 6-31G(d) basis set. For **Xp-mCP** and **Xm-mCP**, the value of ω in the ωB97XD functional was optimized by minimizing the value of J^2,

$$J^2 = \left(-\varepsilon_{\mathrm{HOMO}} + E_{\mathrm{IE}}\right)^2 + \left(-\varepsilon_{\mathrm{LUMO}} + E_{\mathrm{EA}}\right)^2$$

where $\varepsilon_{\mathrm{HOMO}}$ and $\varepsilon_{\mathrm{LUMO}}$ are the HOMO and LUMO energy levels of a given molecule, respectively; E_{IE} and E_{EA} represent the ionization energy and electron affinity, respectively. The optimal ω values (ω^*) for **Xp-mCP** and **Xm-mCP** were determined to be 0.004 and 0.005 Bohr^{-1}, respectively. Finally, the S_1 and T_1 energies of **Xp-mCP** and **Xm-mCP** were directly calculated by using the time-dependent DFT (TD-DFT) with the ω^*B97XD functional and 6-31G(d) basis set. In addition, the natural transition orbitals (NTOs) were calculated for the absorption transitions from the singlet ground state (S_0) to higher singlet excited states (S_n).

Single carrier devices

The single-carrier devices of the hole-only device (HOD) and the electron-only device (EOD) were constructed using a clean glass substrate coated with an indium tin oxide (ITO) layer with a sheet resistance of 10 Ω/sq and an active pattern size of 2 × 2 mm^2, acting as the anode. The HOD was fabricated with a configuration of ITO (150 nm)/poly(3,4-ethylenedioxy thiophene):poly(styrenesulfonic acid) (PEDOT:PSS; 40 nm)/poly-(9-vinylcarbazole) (PVK; 10 nm)/xanthone-based host (20 nm)/Al (100 nm), while the EOD was fabricated with ITO (150 nm)/ xanthone-based host (20 nm)/ 1,3,5-tris(1-phenyl-1*H*-benzimidazol-2-yl)benzene (TPBi; 40 nm)/LiF (0.8 nm)/Al (100 nm). The PEDOT:PSS was spin-coated directly on the ITO substrate at a spinning speed of 4000 rpm, and annealed at 155°C for 15 minutes. The PVK was dissolved in

chlorobenzene (0.5 wt% solution) and spin-coated onto the PEDOT: PSS / ITO substrate at a spinning speed of 4000 rpm, and dried at 130 °C for 20 min. Then the two hosts were dissolved in toluene (0.4 wt% solution) and spin-coated as required. The spinning speed was 3000 rpm. Whereas TPBi, LiF, and cathode (Al) was deposited at a base pressure of 1.0×10^{-6} Torr. The deposition rate of TPBi, LiF, and Al were controlled at 1–2 Å/s, 0.1 Å/s, and 5-6 Å/s, respectively.

In HODs, the PEDOT: PSS and PVK acted as the hole injection and transport layers, respectively. The TPBi and LiF acted as the electron transport and injection layers, respectively, in EODs. Finally, the current density-voltage (*J-V*) data were obtained using a Keithley SMU 236 instrument.

Fabrication and characterization of OLEDs

The green-OLED devices were constructed with the configuration of ITO/PEDOT: PSS (40 nm)/ PVK (20 nm)/ EML (15 nm)/TPBi (40 nm)/LiF (0.8 nm)/Al (100 nm).

The emissive layer consisted of the host (**Xp-mCP** or **Xm-mCP**) and t4CzIPN green dopant. An ITO-coated glass with a sheet resistance of 10 Ω/sq and an active pattern area of 2×2 mm^2 was formed as an anode. This ITO-coated glass was washed with distilled water, isopropanol, and dried in a vacuum oven. The PEDOT:PSS layer that functioned as a hole injection layer was spin-coated directly on the ITO substrate and annealed at 155°C for 15 minutes. Then the PEDOT:PSS layer was spin-coated onto the ITO glass substrate at a spinning speed of 4000 rpm, and dried at 150 °C for 10 min. The PVK that functioned as a hole transport layer was dissolved in chlorobenzene (0.5 wt% solution) and directly spin-coated onto PEDOT: PSS / ITO substrate at a spinning speed of 4000 rpm, and dried at 130 °C for 20 min. The emitting layer was formed by spin-coating on the PVK layer from 0.2 wt% toluene solution of xanthone host materials and

t4CzIPN. The spinning speed was 3000 rpm. The electron transport layer (TPBi), the electron injection layer (LiF), and the cathode (Al) were deposited at a base pressure of 1.0×10^{-6} Torr. The deposition rate of TPBi, LiF, and Al were controlled at 1–2 Å/s, 0.1 Å/s, and 5-6 Å/s, respectively. Finally, the current density-voltage-luminance (*J*-*V*-*L*) data were measured by a Keithley SMU 236 instrument and the SpectraScan PR-655 colorimeter. The current efficiency and power efficiency were also calculated by device parameters.

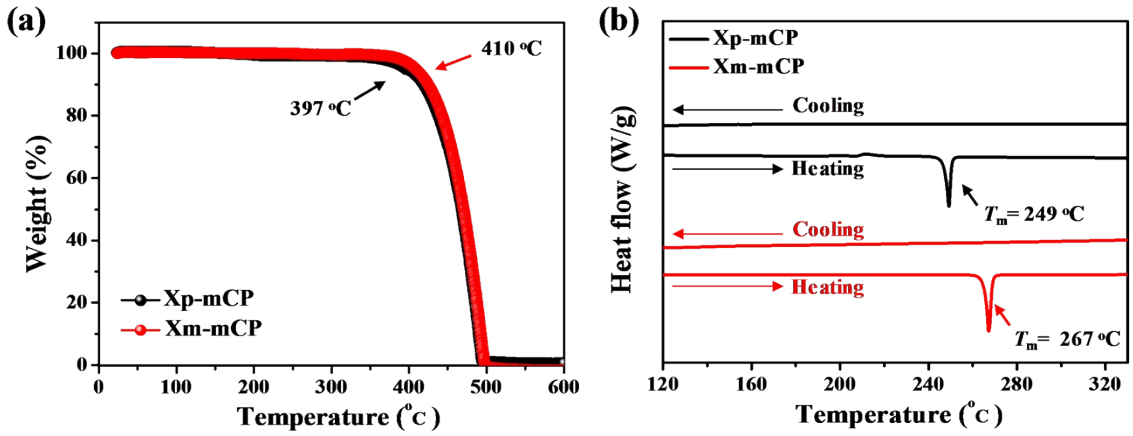

Fig. S1. (a) Thermogravimetric analysis and (b) differential scanning calorimetry curves of **Xp-mCP** and **Xm-mCP** measured at a heating(or cooling) rate of 10℃/min under N_2 atmosphere.

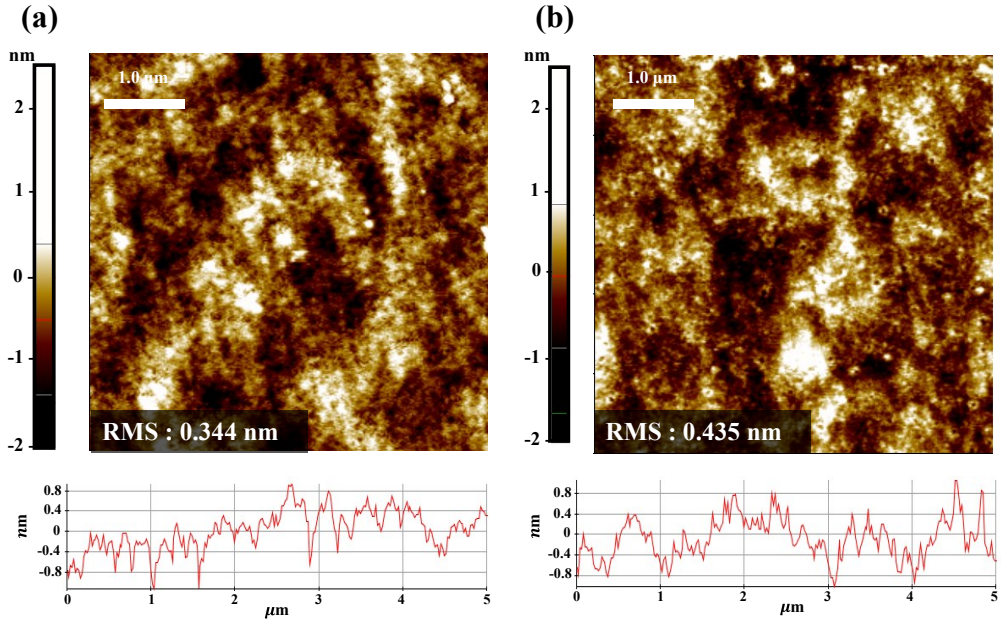

Fig. S2. Atomic force microscopy image and surface profiles of the emitting layer on glass (a) **Xp-mCP** : 20 wt% t4CzIPN (b) **Xm-mCP** : 20 wt% t4CzIPN ($5\mu m \times 5\mu m\ scale$)

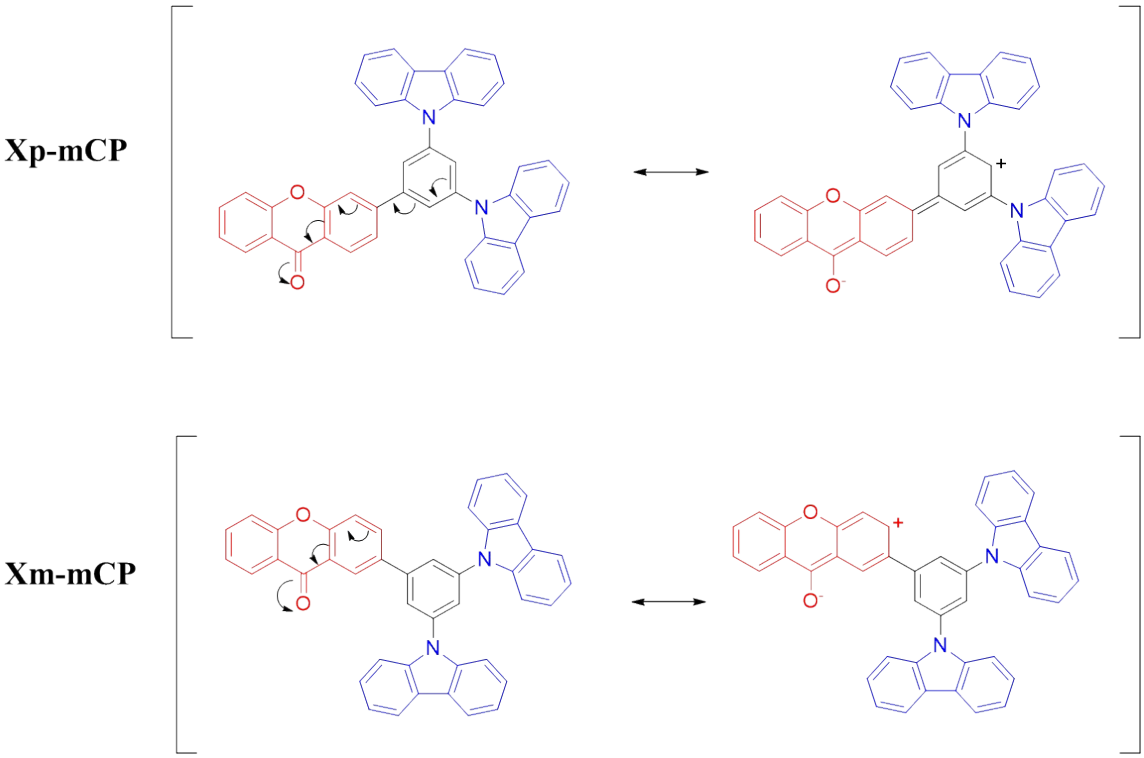

Fig. S3. Resonance structures of **Xp-mCP** and **Xm-mCP**. The conjugation of xanthone in **Xp-mCP** is extended to the phenyl linker. The carbazole donor unit is better separated from the xanthone acceptor unit in **Xm-mCP**.

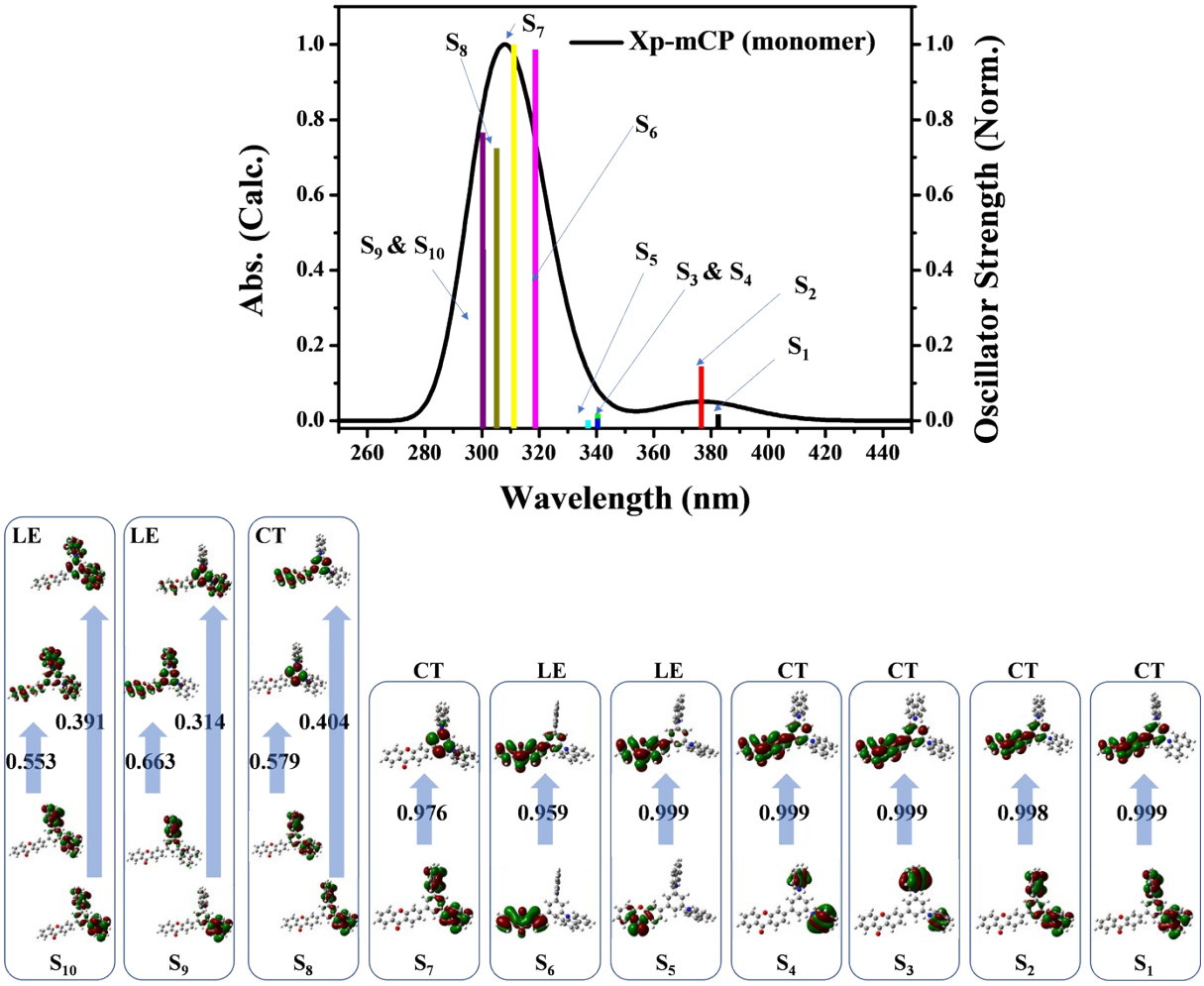

Fig. S4. Calculated absorption spectrum and natural transition orbitals of **Xp-mCP** monomer in toluene.

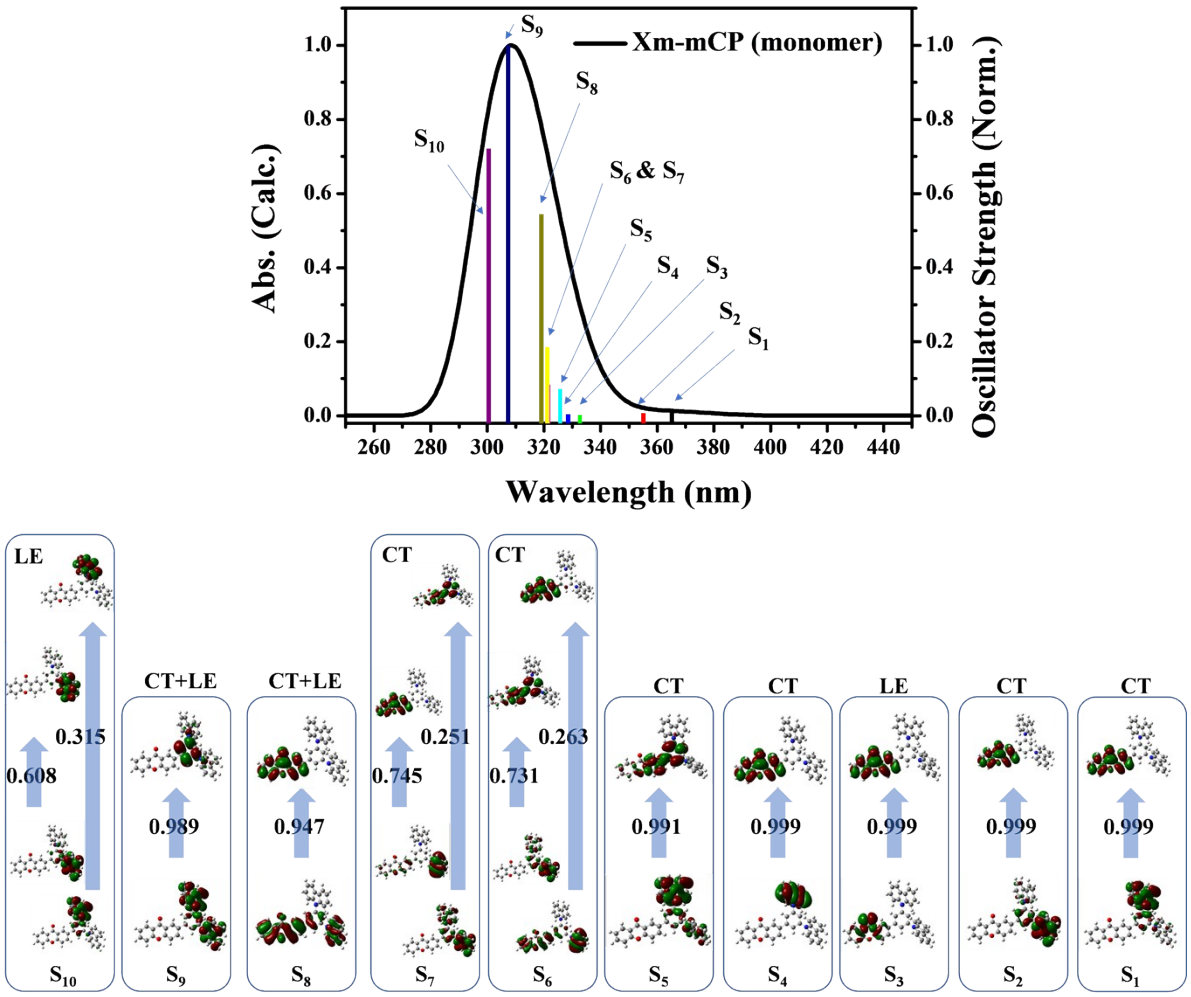

Fig. S5. Calculated absorption spectrum and natural transition orbitals of **Xm-mCP** monomer in toluene.

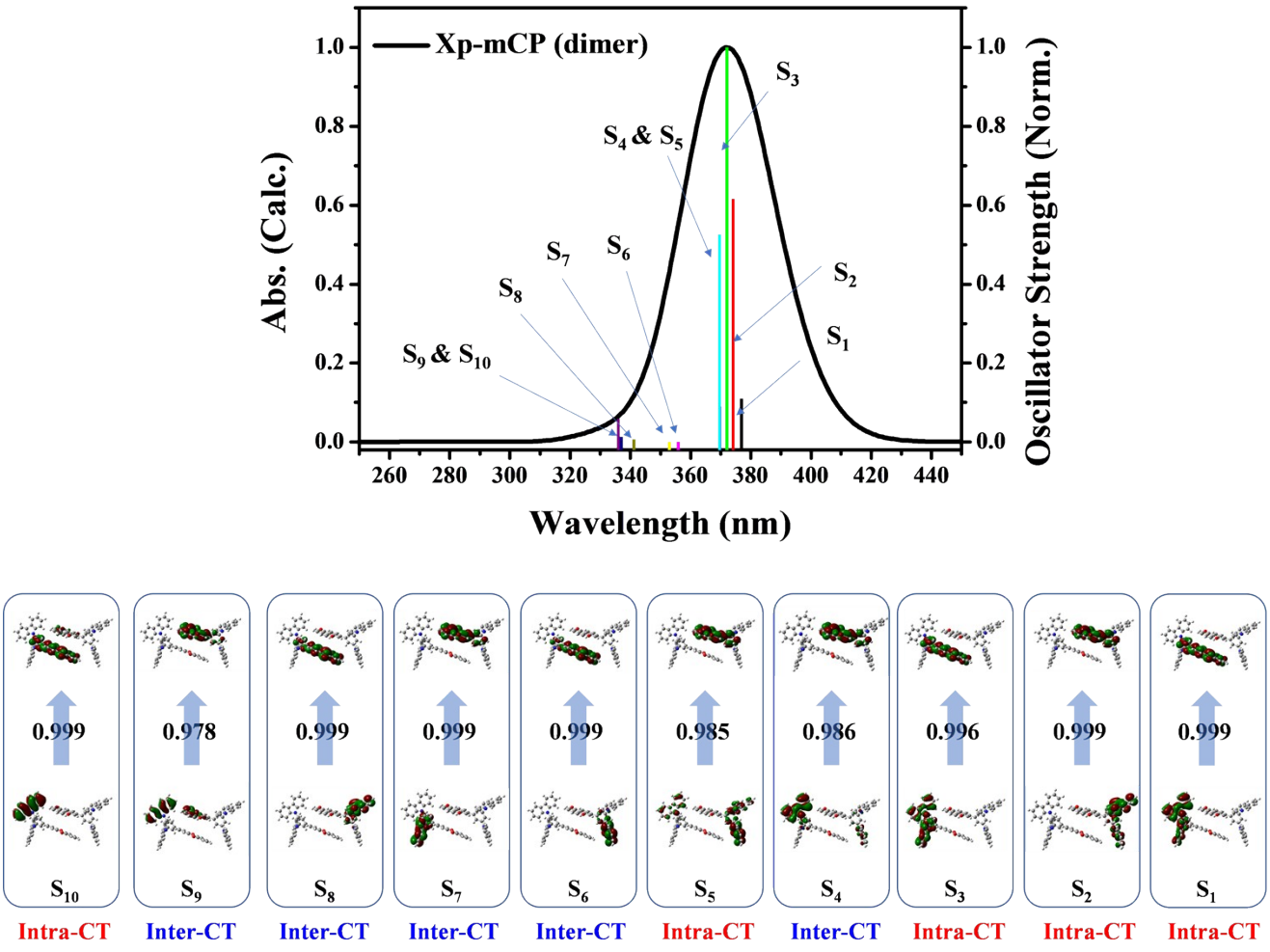

Fig. S6. Calculated absorption spectrum and natural transition orbitals of **Xp-mCP** dimer in toluene.

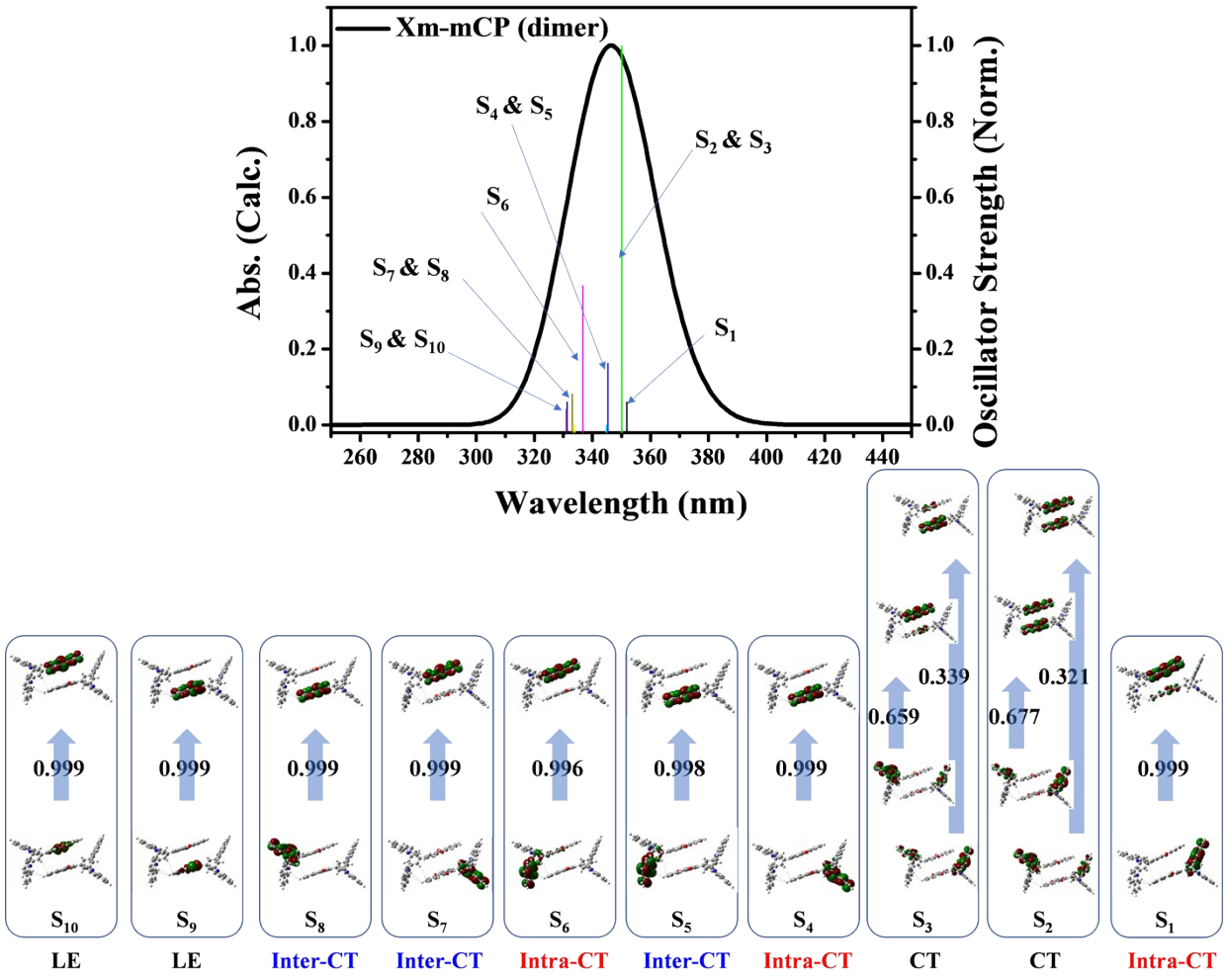

Fig. S7. Calculated absorption spectrum and natural transition orbitals of **Xm-mCP** dimer in toluene.

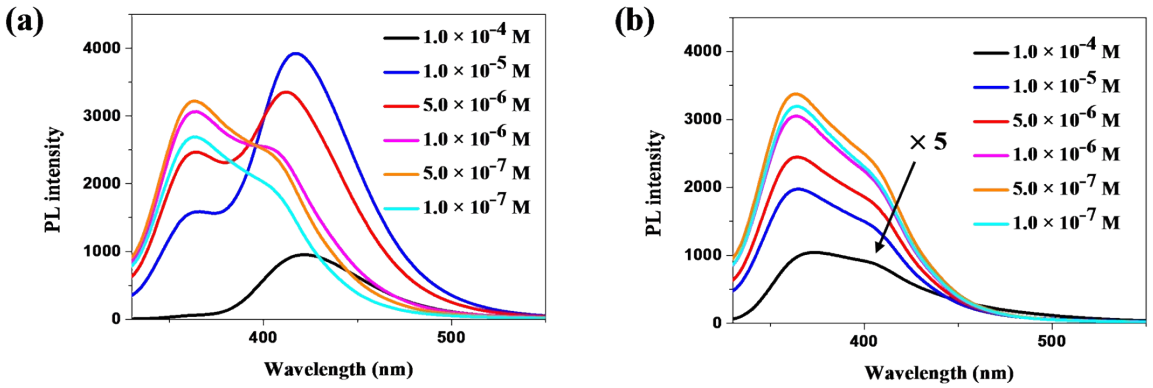

Fig. S8. PL spectra of **Xp-mCP** (a) and **Xm-mCP** (b) in toluene solution of different concentrations.

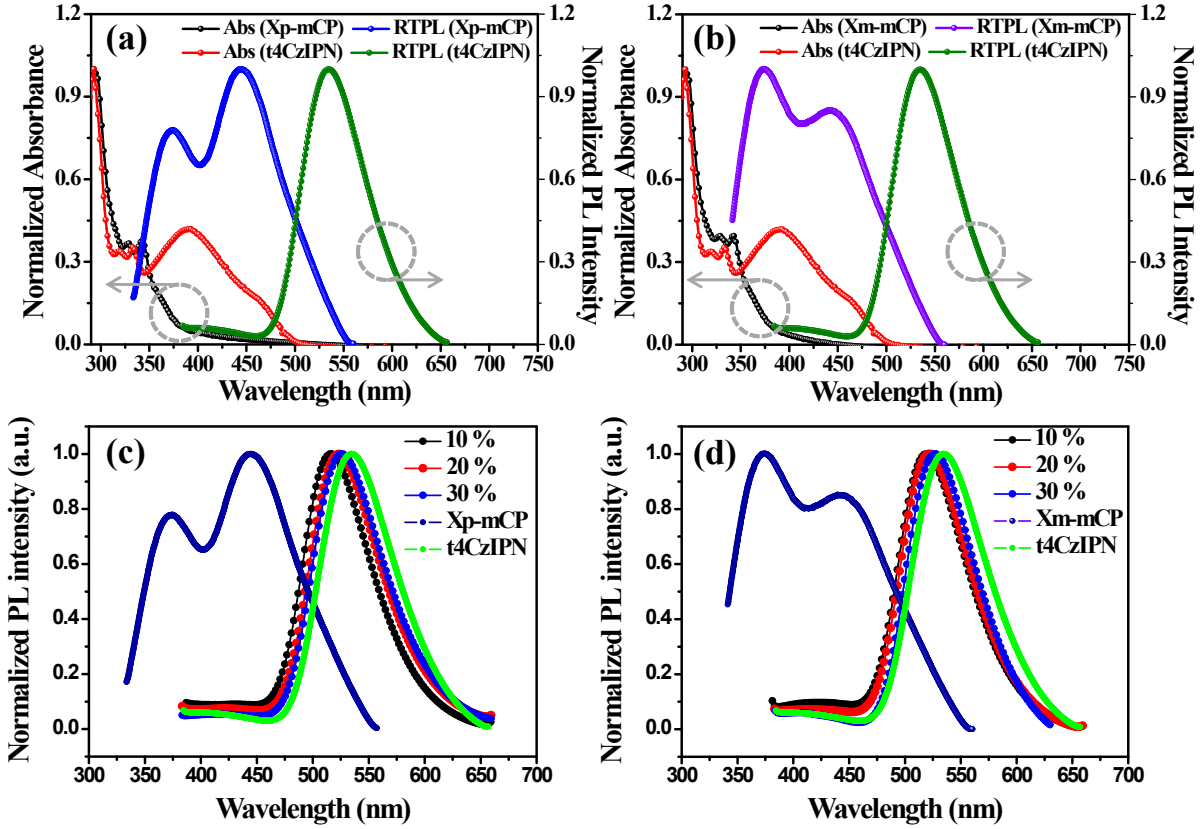

Fig. S9. (a) UV-vis absorption and PL spectra of **Xp-mCP** and t4CzIPN, and (b) UV-vis absorption and PL spectra of **Xm-mCP** and t4CzIPN (c) PL spectra of the doped films of **Xp-mCP** : x wt% t4CzIPN (x = 10, 20 and 30), **Xp-mCP** and t4CzIPN, and (d) PL spectra of the doped films of **Xm-mCP** : x wt% t4CzIPN (x = 10, 20 and 30), **Xm-mCP** and t4CzIPN.

Table S1. Photophysical properties and kinetic parameters of t4CzIPN doped films.

Host	τ_p (ns) [a]	τ_d (μs) [b]	Φ_{PL} (%) [c]	Φ_p (%) [d]	Φ_d (%) [e]	k^S_r (10^7 s^{-1}) [f]	k^S_{nr} (10^7 s^{-1}) [g]	k_{ISC} (10^7 s^{-1}) [h]	k_{RISC} (10^7 s^{-1}) [i]
Xp-mCP	10.0	3.12	65.4	14.4	51.0	1.44	0.762	7.80	0.146
Xm-mCP	10.2	2.65	63.8	11.4	52.4	1.12	0.634	8.05	0.211

[a] Prompt lifetime. [b] Delayed lifetime. [c] Total PLQY. [d] PLQY of prompt fluorescence, and [e] PLQY of delayed fluorescence estimated using the corresponding proportions in the transient decay curve. [f] Radiative decay rate constant of the singlet excited state. [g] Non-radiative decay rate constant for singlet excited state. [h] Intersystem crossing rate constant, [i] Reverse intersystem crossing rate constant.

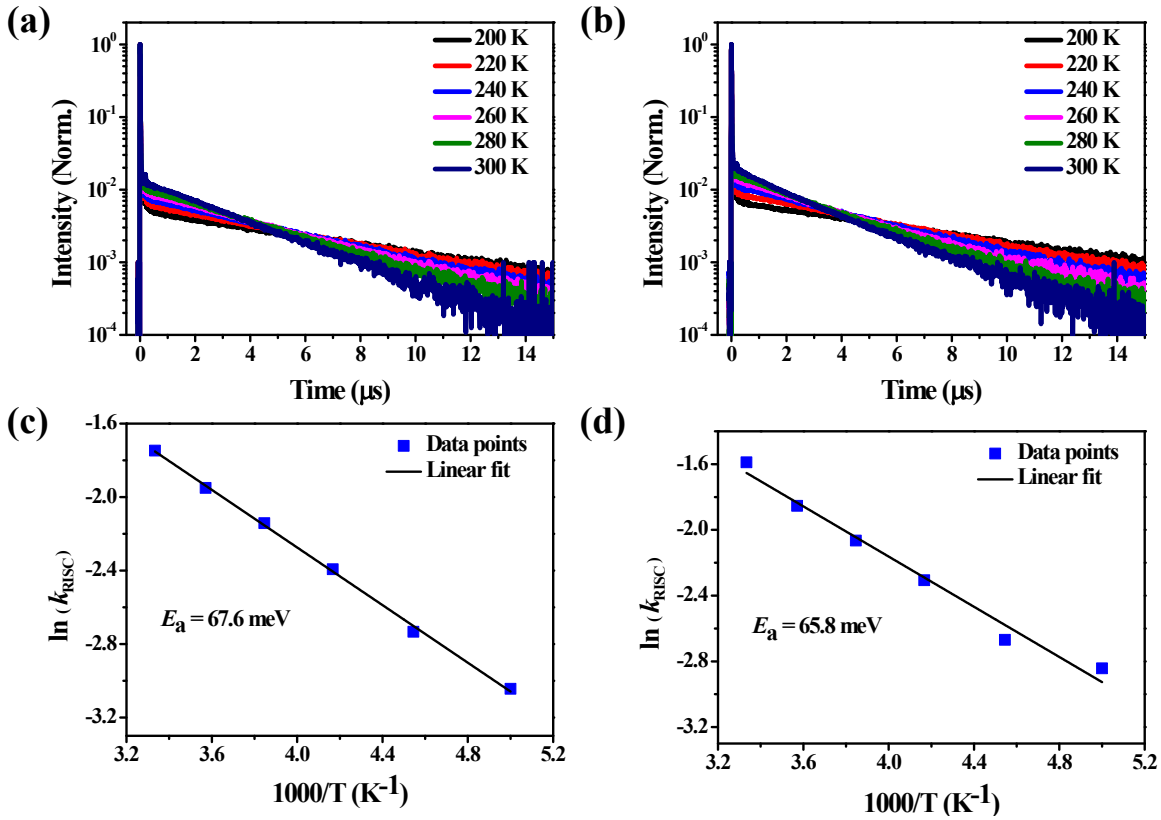

Fig. S10. (a), (b) Time-resolved PL (TRPL) signals of t4CzIPN in the films of **Xp-mCP** and **Xm-mCP** at different temperatures (from 200 K to 300 K with intervals of 20 K). (c), (d) The Arrhenius plots of the reverse intersystem crossing rate constant and the activation energy, E_a, which was determined from the slope of the Arrhenius plot.

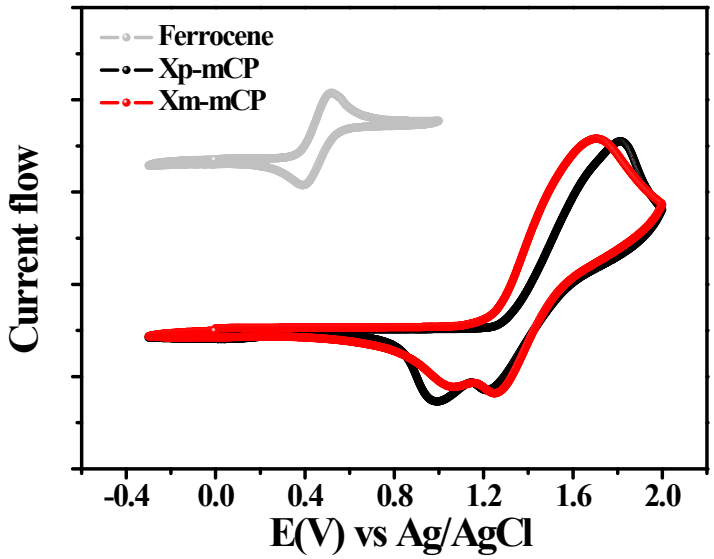

Fig. S11. Cyclic voltammograms of **Xp-mCP** and **Xm-mCP**.

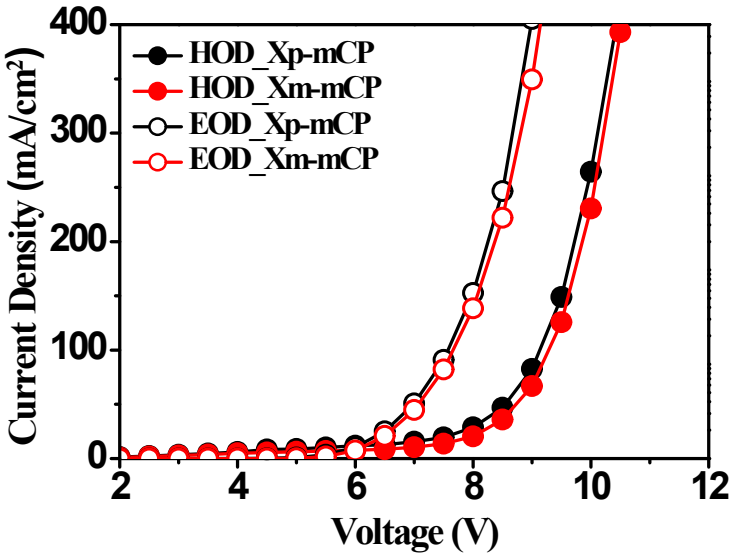

Fig. S12. Curves for hole-only and electron-only devices using **Xp-mCP** and **Xm-mCP** host materials.

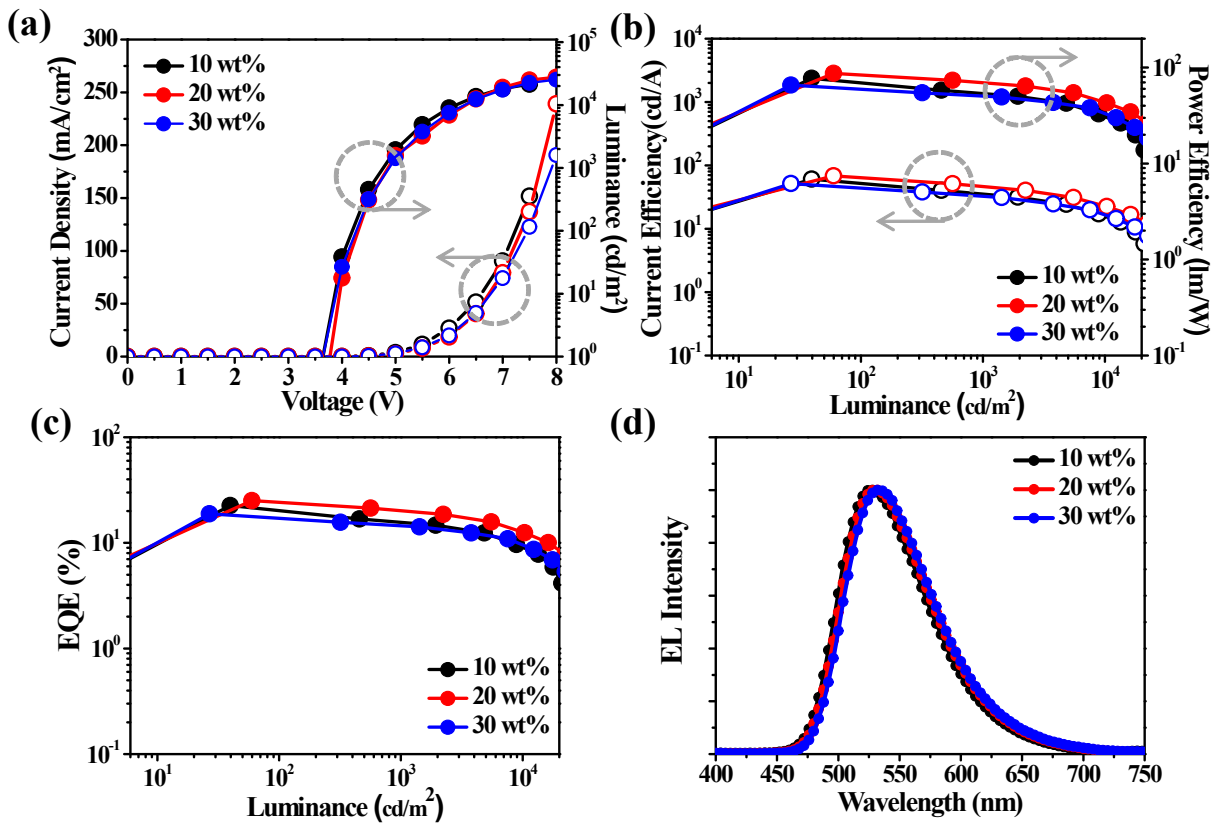

Fig. S13. (a) Current density-voltage-luminance (*J*-*V*-*L*) curves, (b) current efficiency–luminance-power efficiency (CE-*L*-PE) curves, (c) external quantum efficiency-luminance curves, (d) EL spectra of devices at a luminance of 1000 cd m^{-2} for the thermally activated delayed fluorescence-OLEDs devices with **Xp-mCP**:t4CzIPN as the emitting layer (Doping concentration of 10, 20, and 30 wt%).

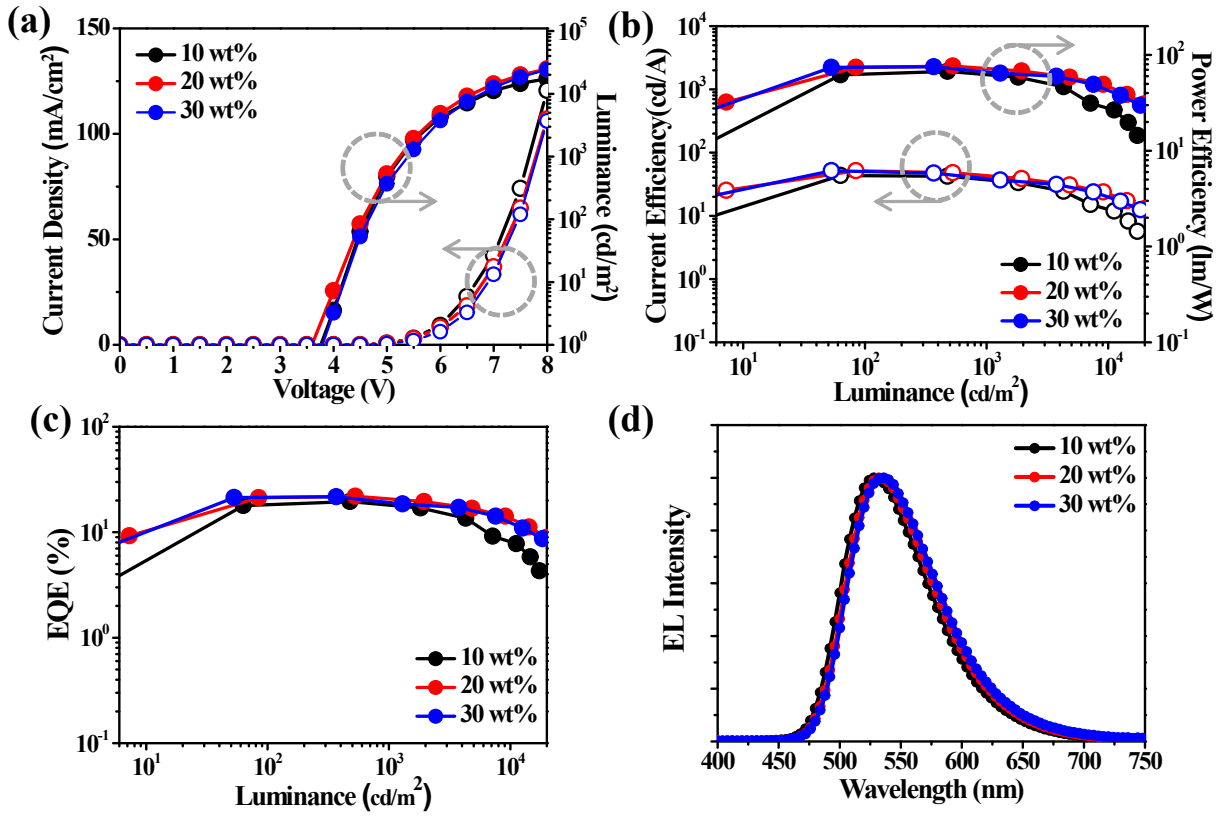

Fig. S14. (a) Current density-voltage-luminance (*J*-*V*-*L*) curves, (b) current efficiency–luminance-power efficiency (CE-*L*-PE) curves, (c) external quantum efficiency-luminance curves, (d) EL spectra of devices at a luminance of 1000 cd m^{-2} for the thermally activated delayed fluorescence-OLEDs devices with **Xm-mCP** : t4CzIPN as the emitting layer (Doping concentration of 10, 20, and 30 wt%).

Table S2. Performance data of solution-processed thermally activated delayed fluorescence - OLEDs based on **Xp-mCP** and **Xm-mCP** with different concentrations of the dopant.

EML	Doping Conc. (wt%)	V_{on} [a] (V)	CE_{max} [b] (cd/A)	PE_{max} [c] (lm/W)	Luminance [d] (cd/m^2)	η_{ext} [e] (%)				EL_{max} [g]	CIE [h] (x, y)
						Max	500 cd m^{-2}	1000 cd m^{-2}	2000 cd m^{-2}		
Xp-mCP :t4CzIPN	10	3.5	56.7	41.1	21520	16.6	16.4 (1.2) [f]	15.8 (4.8) [f]	14.6 (12.0) [f]	528	(0.33, 0.60)
	20	3.5	66.3	47.7	27620	19.3	18.8 (2.6) [f]	18.0 (6.7) [f]	15.7 (18.7) [f]	532	(0.34, 0.60)
	30	3.5	65.6	51.5	25460	18.8	15.5 (17.7) [f]	14.7 (21.8) [f]	13.7 (27.4) [f]	532	(0.35, 0.60)
Xm-mCP :t4CzIPN	10	3.6	67.5	43.3	17400	19.5	19.4 (0.3) [f]	18.6 (4.6) [f]	16.7 (14.4) [f]	528	(0.33, 0.60)
	20	3.5	76.5	51.8	32690	22.0	21.9 (0.5) [f]	21.0 (4.5) [f]	19.5 (11.4) [f]	532	(0.35, 0.59)
	30	3.6	75.3	51.8	30650	21.7	21.2 (2.3) [f]	19.5 (10.1) [f]	18.1 (16.6) [f]	536	(0.36, 0.59)

[a] Turn-on voltage at 1 cd/m^2, [b] Maximum current efficiency. [c] Maximum power efficiency. [d] Maximum luminance. [e] Maximum external quantum efficiency at maximum/500/1000/2000 cd m^{-2}. [f] Roll-off percentage (%). [g] EL peak wavelength. [h] Commission Internationale de L'Eclairage coordinates at 1000 cd m^{-2}.

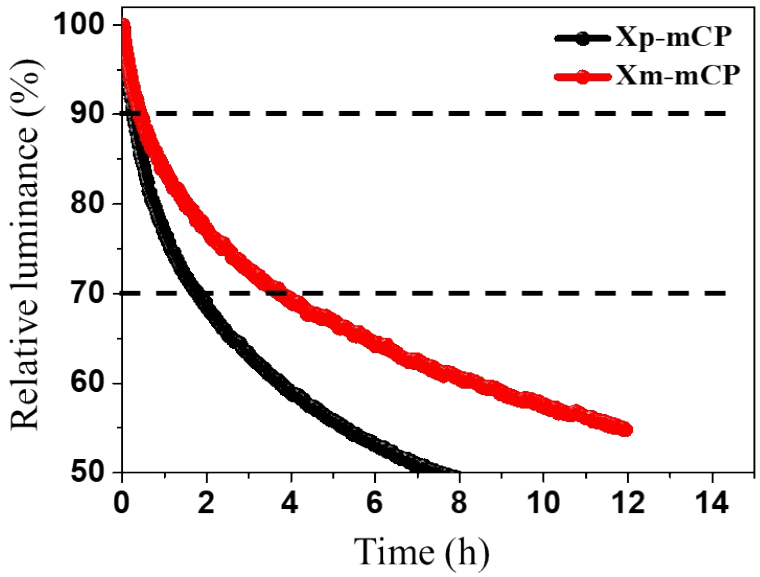

Fig. S15. Lifetime curves of 20 wt% t4CzIPN doped **Xp-mCP** and **Xm-mCP** based devices at an initial luminance of 300 cd m^{-2}.

Table S3. Comparison of the maximum external quantum efficiency and roll-off behavior at 1000 cd m^{-2} for solution-processed green thermally activated delayed fluorescence-OLEDs.

No.	Host	Dopant	EQE (%)		Roll-off (%)	Reference
			max	1000 cd/m^2		
1	**Xp-mCP**	**t4CzIPN**	**19.3**	**18.0**	**6.7**	**In this study**
2	**Xm-mCP**	**t4CzIPN**	**22.0**	**21.0**	**4.5**	**In this study**
3	SiCz	t4CzIPN	18.3	12.0	34.0	5
4	mCPDPO	t4CzIPN	18.8	12.4	34.0	6
5	IAPC	t4CzIPN	19.2	17.5	9.0	7
6	SiCT	t4CzIPN	19.2	12.4	36.0	8
7	mCP	4CzIPN	21.0	<16.0	>24.0	9
8	CBP	4CzIPN	20.0	13.3	33.5	10
9	CBP:PO-T2T	4CzIPN	18.1	14.9	17.7	10
10	Cz-3CzCN	CzCzCN	23.8	12.6	47.0	11
11	*m*-DTPACO	4CzCNPy	13.0	10.3	20.8	12
12	*p*-DTPACO	4CzCNPy	9.0	5.6	37.8	12
13	*p*CNBCzmCF$_3$	4CzCNPy	10.9	8.0	26.6	13
14	TPA-3:PO-T2T	9PhFDPhTz	24.0	10.1	58.0	14

Fig. S16. ^{1}H-NMR spectrum of **Xp-mCP**.

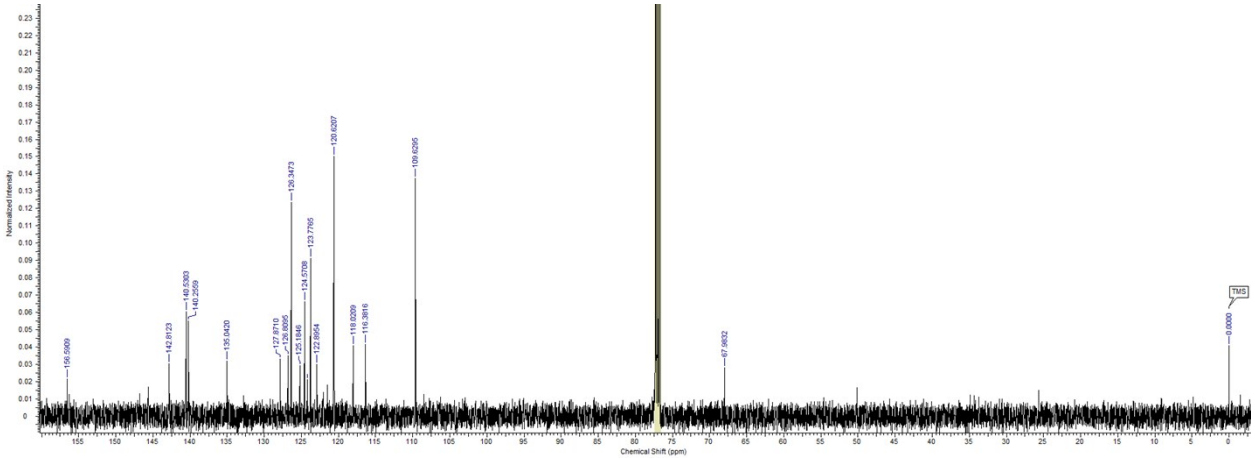

Fig. S17. ^{13}C-NMR spectrum of **Xp-mCP**.

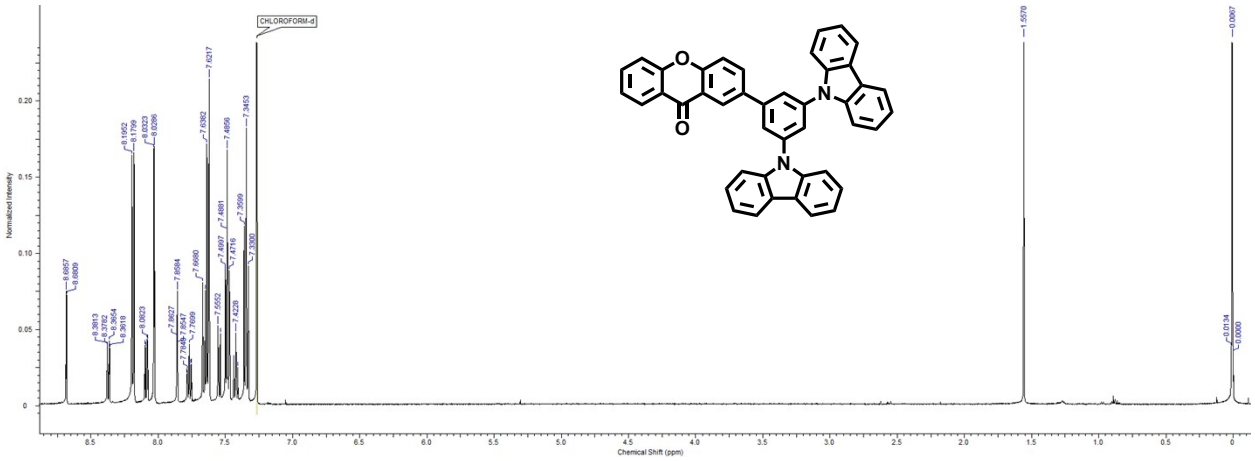

Fig. S18. ^{1}H-NMR spectrum of **Xm-mCP**.

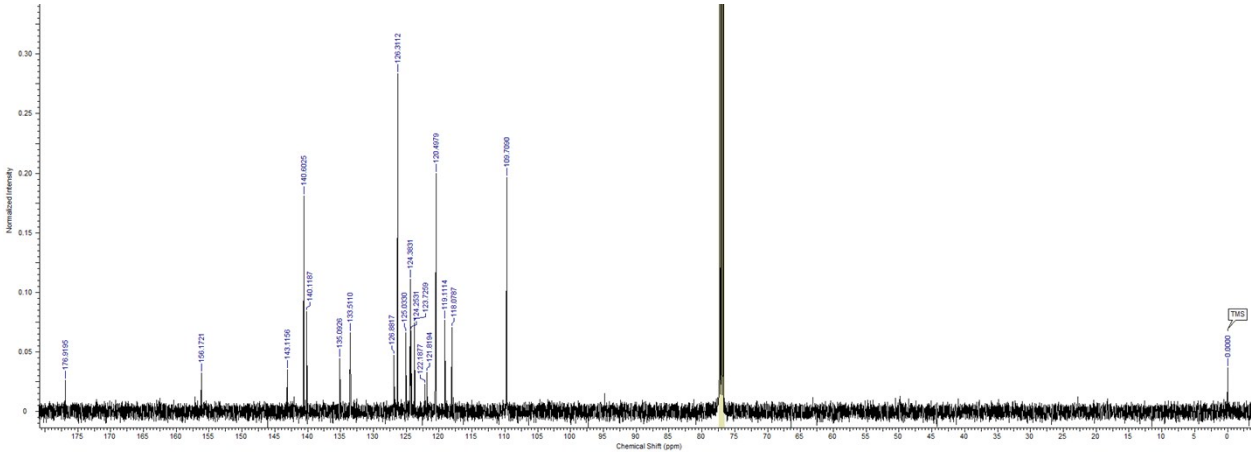

Fig. S19. ^{13}C-NMR spectrum of **Xm-mCP**.

REFERENCES

(1) M. J. Frisch, G. W. Trucks, H. B. Schlegel, G. E. Scuseria, M. A. Robb, J. R. Cheeseman, G. Scalmani, V. Barone, G. A. Petersson, H. Nakatsuji, et al. Gaussian 16 Rev. A.03, Wallingford, CT, 2016.

(2) T. J. Penfold, *J. Phys. Chem. C*, 2015, **119**, 13535-13544.

(3) H. Sun, C. Zhong, J.-L. Brédas, *J. Chem. Theory Comput.*, 2015, **11**, 3851-3858.

(4) P. K. Samanta, D. Kim, V. Coropceanu, J.-L. Brédas, *J. Am. Chem. Soc.*, 2017, **139**, 4042-4051.

(5) Y. J. Cho, K. S. Yook, J. Y. Lee, *Adv. Mater.*, 2014, **26**, 6642-6.

(6) M. Godumala, S. Choi, S. K. Kim, S. W. Kim, J. H. Kwon, M. J. Cho, D. H. Choi, *J. Mater. Chem. C*, 2018, **6**, 10000-10009.

(7) C. H. Jeong, M. Godumala, J. Yoon, S. Choi, Y. W. Kim, D. H. Choi, M. J. Cho, D. H. Choi, *ACS Appl. Mater. Interfaces*, 2019, **11**, 17602-17609.

(8) S. Choi, J. W. Yoon, M. Godumala, H. J. Kim, S. H. Park, S. K. Kim, H. Lee, J. H. Kwon, M. J. Cho, D. H. Choi, *Dyes. Pigm.*, 2019, **167**, 120-126.

(9) T. Zhou, G. Xie, S. Gong, M. Huang, J. Luo, C. Yang, *ACS Appl. Mater. Interfaces*, 2017, **9**, 34139-34145.

(10) H.-Y. Yang, C.-J. Zheng, M. Zhang, J.-W. Zhao, P.-L. Zhong, H. Lin, S.-L. Tao, X.-H. Zhang, *Org. Electron.*, 2019, **73**, 36-42.

(11) X. Ban, A. Zhu, T. Zhang, Z. Tong, W. Jiang, Y. Sun, *Chem. Commun.*, 2017, **53**, 11834-11837.

(12) J. Hu, X. Zhang, D. Zhang, X. Cao, T. Jiang, X. Zhang, Y. Tao, *Dyes. Pigm.*, 2017, **137**, 480-489.

(13) X. Cao, J. Hu, Y. Tao, W. Yuan, J. Jin, X. Ma, X. Zhang, W. Huang, *Dyes. Pigm.*, 2017, **136**, 543-552.

(14) J. Zhao, C. Zheng, Y. Zhou, C. Li, J. Ye, X. Du, W. Li, Z. He, M. Zhang, H. Lin, S. Tao, X. Zhang, *Mater. Horiz.*, 2019, **6**, 1425-1432.